01 Jul 2013

Dynamics and Dislodgment from Pore Constrictions of a Trapped Nonwetting Droplet Stimulated by Seismic Waves

Wen Deng
Missouri University of Science and Technology, wendeng@mst.edu

M. Bayani Cardenas

Recommended Citation

W. Deng and M. B. Cardenas, "Dynamics and Dislodgment from Pore Constrictions of a Trapped Nonwetting Droplet Stimulated by Seismic Waves," *Water Resources Research*, vol. 49, no. 7, pp. 4206-4218, American Geophysical Union (AGU), Jul 2013.
The definitive version is available at https://doi.org/10.1002/wrcr.20335

WATER RESOURCES RESEARCH, VOL. 49, 4206–4218, doi:10.1002/wrcr.20335, 2013

Dynamics and dislodgment from pore constrictions of a trapped nonwetting droplet stimulated by seismic waves

Wen Deng[1] and M. Bayani Cardenas[1]

Received 5 October 2012; revised 15 May 2013; accepted 27 May 2013; published 23 July 2013.

[1] Seismic waves affect fluid flow and transport processes in porous media. Therefore, quantitative understanding of the role of seismic waves in subsurface hydrodynamics is important for the development of practical applications and prediction of natural phenomena. We present a theoretical fluid dynamics model to describe how low-frequency elastic waves mobilize isolated droplets trapped in pores by capillary resistance. The ability of the theoretical model to predict the critical mobilization amplitudes (A_c) and the displacement dynamics of the nonwetting droplet are validated against computational fluid dynamics (CFD) simulations. Our theory has the advantage of rapid calculation of A_c for various scenarios. Both theory and CFD simulations show that the A_c increases with increasing wave frequency. The theoretical and computational models agree well in the low-frequency range both in terms of predicting the displacement history of the droplet and its eventual dislodgment, but their results begin to diverge with increasing wave frequency since the Hagen-Poiseuille flow approximation in the model becomes invalid. Relative to a previous "viscous seismic model," our model compares more favorably to experimental observations. The model is thus appropriate for predicting trapped nonwetting droplet dynamics in and dislodgement from pore constrictions by low-frequency elastic waves.

Citation: Deng, W., and M. B. Cardenas (2013), Dynamics and dislodgment from pore constrictions of a trapped nonwetting droplet stimulated by seismic waves, *Water Resour. Res.*, *49*, 4206–4218, doi:10.1002/wrcr.20335.

1. Introduction

[2] Seismic waves generated by earthquakes have been observed to cause dynamic changes in hydraulic behavior of porous media. Specifically, elastic waves affect permeability [*Elkhoury et al*., 2006, 2011; *Geballe et al*., 2011; *Liu and Manga*, 2009; *Manga et al*., 2012; *Wang and Manga*, 2010], release trapped colloidal particles by low-frequency stress stimulation [*Beckham et al*., 2010; *Roberts and Abdel-Fattah*, 2009; *Thomas and Chrysikopoulos*, 2007], and mobilize capillary trapped nonwetting droplets and bubbles by the addition of seismic wave-induced fictitious force to the background pressure gradient [*Beresnev et al*., 2005; *Iassonov and Beresnev*, 2008; *Li et al*., 2005].

[3] The mobilization of nonwetting droplets and bubbles has long been of practical interest. It can be one of the underlying mechanisms for permeability changes observed after earthquakes [*Manga et al*., 2012]. Moreover, the phenomenon has potential applications in the remediation of aquifers contaminated by nonaqueous phase liquids [*Roberts et al*., 2001] and in enhanced oil recovery [*Beresnev and Johnson*, 1994; *Dobronravov*, 2002; *Kouznetsov et al*., 1998; *Nikolaevskiy et al*., 1996; *Poesio et al*., 2002; *Roberts*, 2005; *Roberts et al*., 2003]. On the other hand, a negative consequence of droplet mobilization can be the reduction of residually trapped CO_2 in saline aquifers; residual trapping is one of the major CO_2 trapping mechanisms for geologic carbon sequestration. The mobilization of CO_2 may be particularly relevant in a CO_2 injection scenario since the injection itself may cause earthquakes [*Zoback and Gorelick*, 2012].

[4] *Iassonov and Beresnev* [2003] established a yield stress model to estimate the effect of low-frequency sound on the flow of fluids in straight tubes with circular cross sections. The straight-tube model does not accurately represent oil entrapment mechanics, and the model falls short of explaining the capillary entrapment in realistic constricted channels. Other studies of vibration-induced phenomena have also considered the resonance of droplets. *Hilpert et al*. [2000] and *Hilpert* [2007] sought to calculate the resonant frequency of trapped oil ganglia under the effect of elastic wave excitation. Resonant mobilization could be a very efficient way to mobilize trapped nonwetting residues with a low requirement in the input seismic energy.

[5] *Beresnev et al*. [2005] recently presented a basic mechanism for elastic wave stimulation in constricted pores: they proposed that there is an "unplugging" threshold whose exceedance would lead to flow of the nonwetting ganglia past constrictions and that this threshold can be exceeded by addition of a sufficiently large oscillatory fictitious force to the external pressure gradient.

Additional supporting information may be found in the online version of this article.

[1]Department of Geological Sciences, University of Texas at Austin, Austin, Texas, USA.

Corresponding author: W. Deng, Department of Geological Sciences, The University of Texas at Austin, Austin, TX 78712, USA. (wendeng@utexas.edu)

0043-1397/13/10.1002/wrcr.20335

[6] *Li et al*. [2005] showed evidence which supported the suggested mobilization mechanism in a specially designed two-dimensional (2-D) micromodel laboratory experiment, and the mobilization mechanism was later incorporated by *Pride et al*. [2008] into 2-D Lattice Boltzmann computer simulations. Others sought to analyze trapped droplet dynamics and mobilization using computational fluid dynamics (CFD) modeling. *Graham and Higdon* [2000] and *Beresnev et al*. [2005] developed CFD models to simulate the two-phase flow of wetting/nonwetting fluids under vibrational action in one-dimensional sinusoidal axisymmetric channels. They were the first to quantitatively demonstrate that vibrations can indeed unplug the trapped nonwetting phase. However, although CFD simulations are useful, they are inefficient since they require enormous computational resources.

[7] In order to explain the physics of fluid entrapment beyond that which can be explicitly revealed by computational models, *Beresnev* [2006] developed a physics-based theory that could be used to calculate the mobilization conditions. However, the theory assumed that the trapped droplet was completely lubricated by the water film; the viscous resistance of the film was ignored. *Beresnev and Deng* [2010] later improved this theory by considering viscosity effects. Nonetheless, the model, hereafter referred to as the "viscous seismic model," still came with key simplifications. It assumed a constant length for the bubble moving through a channel with a variable profile. This assumption does not hold in real channels with convergent-divergent geometry. The model also ignored the complex pressure distribution along the annular film of water lining the channel's wall, although this pressure is a significant component of the total force balance. Further, a constant pressure gradient was assumed for the two-phase flow, which has not been observed in single-pore laboratory experiments or CFD simulations. Here, we pursue a theoretical model that is free from the above restrictions yet fast in calculating the effect of elastic waves on trapped nonwetting droplet in convergent-divergent pores.

2. Theoretical Fluid Dynamics Model

2.1. Problem Statement

[8] Our primary interest is the effect of vibrations or seismic waves on the trapping of residual nonwetting fluid. The acceleration amplitude and frequency of the vibration are, therefore, the two properties of the seismic wave we focus on.

[9] Nonwetting residues are trapped mainly due to the capillary resistance. According to the Young-Laplace equation, interfacial tension σ and contact angle θ determine the capillary pressure. When ganglia are trapped, the force due to the background pressure gradient in the reservoirs is unable to overcome the counteracting capillary resistance. The capillary resistance in this paper is not the same as the capillary pressure, which is the pressure difference between the wetting and nonwetting phases. The capillary resistance on the droplet is due to the convergent-divergent shape of the pore and results in the imbalance of capillary pressure between the upstream and downstream menisci; the capillary resistance is a capillary pressure difference. The background pressure gradient can be caused either by the natural pressure distribution existing in the geologic reservoir or by injection of fluids such as in water flooding for oil recovery/environmental remediation situations.

[10] The unplugging threshold gradient which needs to be exceeded to free the ganglion is theoretically determined only by the capillary resistance and is normally insensitive to the viscous resistance of a fluid deforming due to shear stress. If the ganglion is being mobilized under the "unplugging" threshold gradient, the passage of the ganglion through the pore throat can be very slow, and the viscous resistance or the shear stress, which is proportional to the radial velocity gradient, is so small that it can be neglected. As long as the pressure gradient is greater than this unplugging threshold, a Newtonian fluid will always be unplugged no matter how slow the flow is. For clarity, we define some basic terminology: "pore neck" is the constricted portion of the pore, and the narrowest section of the neck is the "pore throat."

[11] When a seismic wave passes through a porous medium, an oscillatory fictitious force is added to the background pressure gradient which may cause the counteracting trapping capillary resistance to be overcome. The response of the nonwetting phase to the oscillatory force, whose magnitude and direction are transient, is different to its response to a static pressure gradient. Since the oscillatory motion of the ganglion is naturally transient, the role of viscous resistance in the dissipation of energy cannot be neglected. Viscosity controls how fast the ganglion passes through the pore throat and, therefore, determines whether the ganglion will be freed. A wetting film could also deposit between the nonwetting core fluid and wall. Further, the viscosity ratio of the nonwetting and wetting fluids determines whether the film will behave as a lubricating fluid or a resisting fluid inducing drag. The viscosities of both wetting and nonwetting fluids are thus important parameters considered in the development of our model. Moreover, both wetting and nonwetting fluids are assumed to be incompressible and Newtonian. The yield stress of the fluid is also assumed to be zero.

2.2. Model Geometry and Capillary Resistance

[12] Consider a nonwetting droplet trapped in a constricted axisymmetric tube (Figure 1). The middle part of the tube is sinusoidally shaped and is connected to straight tubes on the left and right. The profile of the tube is given by

$$\lambda(x) = \begin{cases} r_{\max}, & L_1 \le x < -L \\ r_{\min}\left[\dfrac{r_{\max}}{r_{\min}} + \left(1 - \dfrac{r_{\max}}{r_{\min}}\right)\left(1 + \cos\left(\pi\dfrac{x}{L}\right)\right)\right], & -L \le x < L \\ r_{\max}, & L \le x < L_2 \end{cases} \tag{1}$$

where $r_{\min}$ and $r_{\max}$ are the minimum and the maximum radii of the tube, respectively, and $2L$ is the spatial wavelength of the sinusoidally curved portion. L_1 and L_2 are the entrance and exit of the tube, respectively.

[13] When the droplet is passing through the tube constriction, the curvature of the upstream meniscus is smaller than that of the downstream meniscus at the neck. This curvature difference causes the flow-resistive capillary resistance, and the droplet may become stuck at the neck.

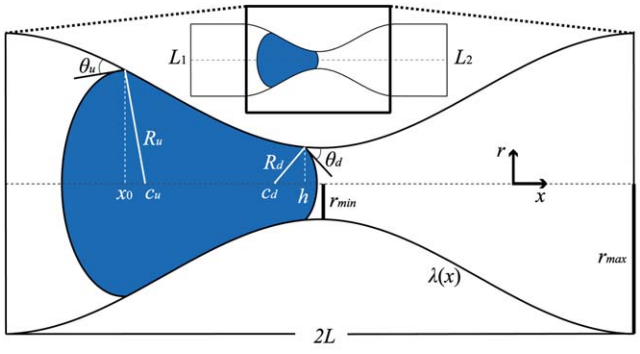

Figure 1. Geometry and spatial parameters of the problem. A nonwetting droplet is initially trapped in the constricted tube. The middle part of the constricted tube is sinusoidally shaped with a wavelength $2L$. Two straight tubes are connected to the left and right of the middle part of the tube.

According to the Young-Laplace equation for a straight tube, the capillary pressure across a two-fluid interface is

$$P_c = \frac{2\sigma\cos\theta}{R} \tag{2}$$

where σ is the wetting/nonwetting fluid interfacial tension, θ is the contact angle, and R is the radius of the tube. The parameter $\cos\theta/R$ is the curvature of the wetting/nonwetting interface. However, the interface curvature is affected by the wall curvature if the tube is not straight. In this case, the capillary pressures are given by

$$\begin{cases} P_{cu} = \dfrac{2\sigma}{R_u(x_u,\theta_u)} \\ P_{cd} = \dfrac{2\sigma}{R_d(x_d,\theta_d)} \end{cases} \tag{3}$$

$$\begin{cases} R_u(x_u,\theta_u) = \dfrac{\lambda(x_u)}{\cos\left(\arctan\left(\lambda'(x_u)\right)+\theta_u\right)} \\ R_d(x_d,\theta_d) = \dfrac{\lambda(x_d)}{\cos\left(\arctan\left(\lambda'(x_d)\right)-\theta_d\right)} \end{cases} \tag{4}$$

where P_{cu} and P_{cd} are the capillary pressures upstream and downstream, R_u and R_d are the radii of curvature of the upstream and downstream menisci, θ_u and θ_d are the contact angles upstream and downstream, and $\lambda'(x)$ is the first spatial derivative of wall profile $\lambda(x)$. As described above, the capillary resistance is actually the capillary pressure difference between the upstream and downstream menisci. Therefore, the capillary resistance is given by

$$\Delta P_c = 2\sigma\left(\frac{1}{R_d(x_d,\theta_d)} - \frac{1}{R_u(x_u,\theta_u)}\right) \tag{5}$$

2.3. Governing Equations and Theoretical Development

[14] In order to describe the transient motion of a nonwetting droplet responding to oscillatory forcing, we employ the macroscopic momentum balance equation for the droplet [*Gauglitz and Radke*, 1989]. The nonwetting droplet itself is the moving-and-deforming control volume. We assume that the flow is axisymmetric and that the flow has only the longitudinal velocity component, which is valid within the context of the lubrication approximation. Thus, the axial component of the macroscopic momentum balance equation is

$$\rho_n \frac{\mathrm{d}}{\mathrm{d}t}\int_V \overline{v}_n \mathrm{d}V = F_x + F_p + F_a + P_{nu}A_u - P_{nd}A_d \tag{6}$$

[15] The left-hand side specifies the momentum accumulation term within the control volume V, ρ_n is the density of the nonwetting fluid, and $\overline{v}_n$ is the cross-sectional mean velocity of the nonwetting droplet. On the right-hand side, F_x, F_p, F_a, $P_{nu}A_u$, and $P_{nd}A_d$ denote the viscous drag, the pressure force along the wetting/nonwetting interface (or along the tube wall if there is no film present), the oscillatory fictitious force, the entrance force due to pressure, and the exit force due to pressure, respectively. P_{nu} and P_{nd} are the pressures at the upstream and downstream menisci of the nonwetting fluid, and A_u and A_d are the cross-sectional areas at the three phase contact positions for the upstream and downstream menisci of the nonwetting fluid.

[16] To solve the momentum balance equation (6), we express each term as a function of the position h, the three-phase contact position at the downstream meniscus, and then solve for h (Figure 1). In reservoirs, although turbulence may develop due to high fluid velocity in the vicinity of active wells, we can assume that the flow of the nonwetting fluid elsewhere is laminar with small Reynolds numbers. Together with the small-slope assumption for the wall of the tube, we can apply the classic lubrication approximation [*Gauglitz and Radke*, 1988, 1990]. The Hagen-Poiseuille flow velocity profile is used to approximate the flow of wetting and nonwetting fluids. If the wetting film with a uniform thickness (t_f) is present, the core-annular flow velocity profile is used. By knowing the mean velocity of the droplet at its downstream meniscus, which is dh/dt, we can determine the entire flow velocity field in terms of h. Furthermore, we can calculate both the viscous drag and the pressure force along the wetting/nonwetting interface by knowing the pressure field. The pressure field, in turn, can be calculated based on the velocity field which is assumed to follow Poiseuille flow.

[17] In the following discussion, we show how each term in equation (6) can be expressed as a function of h.

2.3.1. Accumulation of Momentum Within the Control Volume $\left(\rho_n \frac{\mathrm{d}}{\mathrm{d}t}\int_V \overline{v}_n \mathrm{d}V\right)$

[18] The integration in the left-hand side of equation (6) gives the total momentum change of the droplet with respect to time. The volume of the droplet can be divided into three portions: The tail hemisphere, the front hemisphere, and the volume between the two hemispheres. Therefore, we break apart the calculation of the total momentum accumulation term into these components.

[19] To calculate the total momentum of the droplet, we need to first know the mean velocity $\overline{v}_n(x)$ of the nonwetting fluid at any cross-section x. By noting that dh/dt is the mean velocity of the downstream meniscus, the flow rate Q_n^{core} of the downstream meniscus can be given as

$$Q_n^{\text{core}} = \pi\left(\lambda(h) - t_f\right)^2 \frac{\mathrm{d}h}{\mathrm{dt}} \tag{7}$$

[20] Following volume conservation of the core fluid with a uniformly thick film lining between the core fluid and wall, Q_n^{core} is also the flow rate of the core fluid at all points, and $\overline{v}_n(x)$ is thus given by

$$\overline{v}_n(x) = \frac{\left(\lambda(h) - t_f\right)^2}{\left(\lambda(x) - t_f\right)^2} \frac{\mathrm{d}h}{\mathrm{d}t} \tag{8}$$

[21] The velocity is assumed to be uniform throughout the hemispherical volume formed by the menisci: $\mathrm{d}h/\mathrm{d}t$ for the front and $\mathrm{d}x_0/\mathrm{d}t$ for the tail, the latter of which can be calculated from equation (8), where x_0 is the position of the three-phase contact position at the upstream meniscus (Figure 1). Assuming that local slopes are small, the slope of the interface $\lambda'(x) \sim 0$. The accumulation term for the downstream hemisphere momentum $\mathrm{d}M_d/\mathrm{d}t$ and the upstream hemisphere momentum $\mathrm{d}M_u/\mathrm{d}t$ can thus be given by

$$\frac{\mathrm{d}M_d}{\mathrm{d}t} = \frac{\mathrm{d}\left[\frac{2}{3}\pi\rho_n\left(\lambda(h) - t_f\right)^3 \frac{\mathrm{d}h}{\mathrm{d}t}\right]}{\mathrm{d}t} = \frac{2}{3}\pi\rho_n\left(\lambda(h) - t_f\right)^3 \frac{\mathrm{d}^2h}{\mathrm{d}t^2} \tag{9}$$

$$\begin{aligned}\frac{\mathrm{d}M_u}{\mathrm{d}t} &= \frac{\mathrm{d}\left[\frac{2}{3}\pi\rho_n\left(\lambda(x_0) - t_f\right)^3 \frac{\left(\lambda(h) - t_f\right)^2 \mathrm{d}h}{\left(\lambda(x_0) - t_f\right)^2 \mathrm{d}t}\right]}{\mathrm{d}t} \\ &= \frac{2}{3}\pi\rho_n\left(\lambda(h) - t_f\right)^2\left(\lambda(x_0) - t_f\right)\frac{\mathrm{d}^2h}{\mathrm{d}t^2}\end{aligned} \tag{10}$$

[22] We then substitute $\overline{v}_n(x)$ into the accumulation of the momentum of the volume between the two hemispheres ($\rho_n \frac{\mathrm{d}}{\mathrm{d}t}\int_{x_0}^{h} \overline{v}_n \mathrm{d}V$). The substitution of $\overline{v}_n(x)$ leads to

$$\begin{aligned}\rho_n \frac{d}{dt}\int_{x_0}^{h} \overline{v}_n \mathrm{d}V = {} & \pi\rho_n\left(\lambda(h) - t_f\right)^2 (h - x_0)\frac{\mathrm{d}^2h}{\mathrm{d}t^2} \\ & + \pi\rho_n\left(\lambda(h) - t_f\right)^2\left(1 - \frac{\left(\lambda(h) - t_f\right)^2}{\left(\lambda(x_0) - t_f\right)^2}\right)\left(\frac{\mathrm{d}h}{\mathrm{d}t}\right)^2\end{aligned} \tag{11}$$

[23] Combining equations (9)–(11) together, we yield the total momentum accumulation term of the droplet as

$$\begin{aligned}&\rho_n \frac{\mathrm{d}}{\mathrm{d}t}\int_V \overline{v}_n \mathrm{d}V = \pi\rho_n\left(\lambda(h) - t_f\right)^2 \cdot \\ &\left[h - x_0 + \frac{2}{3}\left(\lambda(x_0) + \lambda(h) - 2t_f\right)\right]\frac{\mathrm{d}^2h}{\mathrm{d}t^2} + \pi\rho_n \\ &\left(\lambda(h) - t_f\right)^2\left(1 - \frac{\left(\lambda(h) - t_f\right)^2}{\left(\lambda(x_0) - t_f\right)^2}\right)\left(\frac{\mathrm{d}h}{\mathrm{d}t}\right)^2\end{aligned} \tag{12}$$

where the volumes occupied by the front and tail menisci are assumed to be that of a hemisphere for simplicity. (However, we use the precise representation of this volume in equation (47) when we calculate the total volume of the droplet to satisfy volume conservation.)

2.3.2. Viscous Drag (F_x)

[24] A straight cylindrical core-annular flow has the velocity profile [*Middleman*, 1995]

$$v_n^{\text{core}}(r) = -\frac{\nabla P}{4\mu_n}\left(R_1^2 - r^2\right) - \frac{\nabla P}{4\mu_w}\left(R_2^2 - R_1^2\right) \tag{13}$$

for the nonwetting core

$$v_w^{\text{film}}(r) = -\frac{\nabla P}{4\mu_w}\left(R_2^2 - r^2\right) \tag{14}$$

for the wetting film/annulus where μ_n and μ_w are the dynamic viscosities of the nonwetting and wetting fluids, R_1 and R_2 are the radii of the fluid/fluid interface and the pore wall, respectively (i.e., $R_2 - R_1 = t_f$), and δP is the external pressure gradient. The core-annular flow velocity profile follows the Hagen-Poiseuille flow velocity profile when $t_f \to 0$. If the oscillatory fictitious force $-\rho a(t)$ (ρ is the density of the fluid and $a(t)$ is the acceleration of the vibrating tube), which is conceptually similar to the gravitational body force $-\rho g$ but applied instead in the horizontal direction (Figure 1), is parallel to the flow and the external gradient δP, it is simply considered as additional forcing. Taking this into account, the velocity profile can be generalized to

$$\begin{aligned}v_n^{\text{core}}(r) = {} & -\frac{\left(\rho_n a(t) + \nabla P_n\right)}{4\mu_n}\left(R_1^2 - r^2\right) \\ & -\frac{\left(\rho_w a(t) + \nabla P_w\right)}{4\mu_w}\left(R_2^2 - R_1^2\right)\end{aligned} \tag{15}$$

for the nonwetting core, and

$$v_w^{\text{film}}(r) = -\frac{\left(\rho_w a(t) + \nabla P_w\right)}{4\mu_w}\left(R_2^2 - r^2\right) \tag{16}$$

for the wetting film, where ρ_w is the density of the wetting fluid. ∇P_n and ∇P_w are the pressure gradients within the core and the film, respectively. To satisfy shear stress continuity at the wetting/nonwetting interface, $\rho_n a(t) + \nabla P_n$ should be equal to $\rho_w a(t) + \nabla P_w$.

[25] By integrating equations (15) and (16) in the axisymmetric tube following the lubrication approximation, we obtain the flow rate for the core and the film (Q_w^{film}) fluids

$$\begin{aligned}Q_n^{\text{core}} = {} & -\frac{\pi\left(\rho_n a(t) + \nabla P_n\right)}{8\mu_n}\left(\lambda(x) - t_f\right)^4 \\ & -\frac{\pi\left(\rho_w a(t) + \nabla P_w\right)}{4\mu_w}\left(\lambda(x) - t_f\right)^2\left(\lambda^2(x) - \left(\lambda(x) - t_f\right)^2\right)\end{aligned} \tag{17}$$

$$\begin{aligned}Q_w^{\text{film}} = {} & -\frac{\pi\left(\rho_w a(t) + \nabla P_w\right)}{4\mu_w} \cdot \\ & \left(\lambda^2(x)\left(\lambda^2(x) - \left(\lambda(x) - t_f\right)^2\right) - \frac{\left(\lambda^4(x) - \lambda(x) - t_f\right)^4}{2}\right)\end{aligned} \tag{18}$$

and the total flow rate

$$\begin{aligned}Q = {} & Q_n^{\text{core}} + Q_n^{\text{film}} \\ = {} & -\frac{\pi\left(\rho_w a(t) + \nabla Pw\right)}{8\mu_w}\left(\lambda^4(x) - \left(\lambda(x) - t_f\right)^4\right) \\ & -\frac{\pi\left(\rho_n a(t) + \nabla P_n\right)}{8\mu_n}\left(\lambda(x) - t_f\right)^4\end{aligned} \tag{19}$$

[26] By simultaneously solving equations (7), (17), and (19), we obtain the total flow rate in terms of h

$$Q = S(h)\frac{\mathrm{d}h}{\mathrm{d}t} \tag{20}$$

where we define

$$S(x) = \pi\frac{\frac{\mu_n}{\mu_w}\left(\lambda^4(x) - \left(\lambda(x) - t_f\right)^4\right) + \left(\lambda(x) - t_f\right)^4}{2\frac{\mu_n}{\mu_w}\left(\lambda^2(x) - \left(\lambda(x) - t_f\right)^2\right) + \left(\lambda(x) - t_f\right)^2} \tag{21}$$

[27] The total force due to shear stress acting along the wetting/nonwetting interface is given by the integration below and utilizing the known velocity profile [*Gauglitz and Radke*, 1989]

$$F_x = \int_{x_0}^{h} \tau_i 2\pi\left(\lambda(x) - t_f\right)\mathrm{d}x \tag{22}$$

where τ_i is the shear stress at the wetting/nonwetting interface, which is determined by the velocity profile of equation (15) and the flow rate equation (17)

$$\tau_i = -\frac{4\mu_n\left(\lambda - t_f\right)\overline{v}_n}{2\frac{\mu_n}{\mu_w}\left(\lambda^2 - \left(\lambda - t_f\right)^2\right) + \left(\lambda - t_f\right)^2} \tag{23}$$

[28] Substitution of τ_i and equation (8) for $\overline{v}_n$ into equation (22) leads to

$$F_x = -8\pi\mu_n\left(\lambda(h) - t_f\right)^2 \mathrm{int}\,1(h)\frac{\mathrm{d}h}{\mathrm{d}t} \tag{24}$$

where int1(x) is defined by

$$\mathrm{int}\,1(x) = \int_{x_0}^{x} \frac{1}{2\frac{\mu_n}{\mu_w}\left(\lambda^2(\xi) - \left(\lambda(\xi) - t_f\right)^2\right) + \left(\lambda(\xi) - t_f\right)^2}\mathrm{d}\xi \tag{25}$$

2.3.3. Pressure Force Along the Wall (F_p)

[29] In order to determine the total force due to the pressure along the wetting/nonwetting fluid interface, we need to firstly find the pressure distribution $P(x)$. We can calculate the pressure distribution by using the pressure gradient ∇P which can be calculated from equation (17). ${Q_n}^{\mathrm{core}}$ is proportional to the sum of the pressure gradient and body force, according to equation (17). Further, by assuming that the film is considerably thin we can neglect the second term of equation (17) and it, therefore, becomes clear that ${Q_n}^{\mathrm{core}}$ is also proportional to $(\lambda - t_f)^4$. In order to satisfy volume conservation, the ${Q_n}^{\mathrm{core}}$ is uniform through x at any given time, but changes with time. Thus, the sum of the pressure gradient and body force is inversely proportional to $(\lambda - t_f)^4$, and we therefore obtain

$$\nabla P_n = -\frac{c\cdot\left(\lambda(h) - t_f\right)^2}{\left(\lambda(x) - t_f\right)^4} - \rho_n a(t) \tag{26}$$

where c is a coefficient; $(\lambda(h) - t_f)^2$ is used in equation (26) for the convenience of calculation. When the integral of ∇P from tail to front is added to P_{nu}, one should get the pressure downstream P_{nd} if the flow is perfectly described by two-phase Hagen-Poiseuille flow just like in a cylindrical tube. In order to get the total pressure drop across the droplet correct, we introduce c as a correction term for our case of a constricted pore; we show later how it is calculated. In equation (26), $a(t)$ is given by

$$a(t) = -A\cdot\sin\left(2\pi f t\right) \tag{27}$$

where A is the acceleration amplitude and f is the frequency of the seismic wave.

[30] By integrating equation (26), we get the pressure distribution

$$P(x) = P_{nu} - c\cdot\left(\lambda(h) - t_f\right)^2\int_{x_0}^{x}\frac{1}{\left(\lambda(\xi) - t_f\right)^4}\mathrm{d}\xi - \rho_n a(t)(x - x_0) \tag{28}$$

[31] Substituting $x = h$ into equation (28), we obtain

$$p_{nd} = P_{nu} - c\cdot\left(\lambda(h) - t_f\right)^2\int_{x_0}^{h}\frac{1}{\left(\lambda(\xi) - t_f\right)^4}\mathrm{d}\xi - \rho_n a(t)(h - x_0) \tag{29}$$

[32] Therefore, the coefficient c can be calculated from equation (29)

$$c = \frac{P_{nu} - P_{nd} - \rho_n a(t)(h - x_0)}{\mathrm{int}\,2(h)\left(\lambda(h) - t_f\right)^2} \tag{30}$$

where int2(x) is defined by

$$\mathrm{int}\,2(x) = \int_{x_0}^{x}\frac{1}{\left(\lambda(\xi) - t_f\right)^4}\mathrm{d}\xi \tag{31}$$

[33] Note that the coefficient c needs to be calculated during each time step in numerical computations, so that the pressure distribution stays consistent with the exit pressure, that is, equation (29) is satisfied.

[34] The pressure force along the wetting/nonwetting interface is normal to the interface. As the radial component can be cancelled due to the tube's axisymmetric geometry, the resultant force is directed only axially. Thus, the resultant pressure force can be calculated by integrating equation (28) along the wetting/nonwetting interface [*Gauglitz and Radke*, 1989] leading to

$$\begin{aligned} F_p &= \int_{x_0}^{h} P(x)2\pi\left(\lambda(x) - t_f\right)\lambda'(x)\mathrm{d}x \\ &= \pi P_{nu}\left(\left(\lambda(h) - t_f\right)^2 - \left(\lambda(x_0) - t_f\right)^2\right) - 2\pi c\cdot \\ &\quad \mathrm{int}\,3(h)\left(\lambda(h) - t_f\right)^2 - \pi\rho_n a(t)(h - x_0)\left(\lambda(h) - t_f\right)^2 \\ &\quad +\pi\rho_n a(t)\mathrm{int}\,4(h) \end{aligned} \tag{32}$$

where we define int3(x) and int4(x) as

$$\mathrm{int}\,3(x) = \int_{x_0}^{x}\mathrm{int}\,2(\xi)\left(\lambda(\xi) - t_f\right)\lambda'(\xi)\mathrm{d}\xi \tag{33}$$

$$\mathrm{int}\,4(x) = \int_{x_0}^{x}\left(\lambda(\xi) - t_f\right)^2\mathrm{d}\xi \tag{34}$$

2.3.4. Oscillatory Fictitious Force (F_a)

[35] According to *Beresnev* [2006], the oscillatory fictitious force in the nonwetting fluid is given by

$$F_a = \int_V -\rho_n a(t)\mathrm{d}v = -\pi\rho_n a(t)\mathrm{int}\,4(h) \tag{35}$$

[36] We use the same expression of int4(x) here.

2.3.5. Entrance and Exit Forces Due to Pressure ($P_{nu}A_u$, $P_{nd}A_d$)

[37] Assume that the external pressure difference exerted on the entrance and exit of the tube is fixed. We define P_{w1} and P_{w2} as the pressures exerted on the entrance and exit of the tube for the wetting fluid (not for the nonwetting fluid), respectively, then

$$\Delta P_e = P_{w1} - P_{w2} = \text{constant} \tag{36}$$

[38] Applying the Hagen-Poiseuille flow assumption, similar as in equation (17) with $t_f = 0$, we can obtain the single-phase flow rate with oscillatory force for the wetting phase existing upstream and downstream of the nonwetting droplet, where no nonwetting fluid exists

$$Q_w = -\frac{(\rho_w a(t) + \nabla P_w)}{8\mu_w}\lambda^4(x) \tag{37}$$

where Q_w is equal to the total flow rate Q according to volume conservation. Therefore,

$$\nabla P_w(x) = -\rho_w a(t) - \frac{8\mu_w Q}{\lambda^4(x)} \tag{38}$$

[39] According to equation (3) for the capillary pressure, we can calculate P_{nu} and P_{nd} as

$$P_{nu} = \int_{L_1}^{x_0} \nabla P_w \mathrm{d}x + P_{w1} + \frac{2\sigma}{R(x_0,\theta_u)} \tag{39}$$

$$P_{nd} = -\int_{h}^{L_2} \nabla P_w \mathrm{d}x + P_{w2} + \frac{2\sigma}{R(h,\theta_d)} \tag{40}$$

where L_1 and L_2 are the positions of the tube entrance and exit (Figure 1).

[40] Using equations (20), (38), (39), (40), and the cross-sectional areas A_u and A_d yield

$$P_{nu}A_u = \pi\big(\lambda(x_0) - t_f\big)^2 \cdot \left[P_{wu} - \rho_w a(t)(x_0 - L_1) - \frac{8\mu_w}{\pi}S(h)\frac{\mathrm{d}h}{\mathrm{d}t}\int_{L_i}^{x_0}\frac{1}{\lambda^4(x)}dx + \frac{2\sigma}{R_u(x_0,\theta_u)}\right] \tag{41}$$

$$P_{nd}A_d = \pi(\lambda(h) - t_f)^2 \cdot \left[P_{wd} + \rho_w a(t)(L_2 - h) + \frac{8\mu_w}{\pi}s(h)\frac{\mathrm{d}h}{\mathrm{d}t}\int_{h}^{L_2}\frac{1}{\lambda^4(x)}\mathrm{d}x + \frac{2\sigma}{R_d(h,\theta_d)}\right] \tag{42}$$

2.3.6. Final Governing Equation for Comprehensive Momentum Balance

[41] Substituting each term from equations (12), (24), (32), (35), (41), and (42) back into equation (6) results in

$$\begin{aligned}&\rho_n\left[h - x_0 + \frac{2}{3}\big(\lambda(x_0) + \lambda(h) - 2t_f\big)\right]\frac{\mathrm{d}^2h}{\mathrm{d}t^2} \\ &+\rho_n\left(1 - \frac{\big(\lambda(h) - t_f\big)^2}{\big(\lambda(x_0) - t_f\big)^2}\right)\left(\frac{\mathrm{d}^2h}{\mathrm{d}t^2}\right) + 8\mu_n\mathrm{int}\,1(h)\frac{\mathrm{d}h}{\mathrm{d}t} = \\ &\Delta P_e - \Delta P_c - \frac{8\mu_w}{\pi}S(h)\frac{\mathrm{d}h}{\mathrm{d}t}\left(\int_{L_1}^{x_0}\frac{1}{\lambda^4(x)}\mathrm{d}x + \int_{h}^{L_2}\frac{1}{\lambda^4(x)}\mathrm{d}x\right) \\ &-2c\cdot\mathrm{int}\,3(h) + \rho_n A\cdot\sin(2\pi ft) \\ &(h - x_0) + \rho_w A\cdot\sin(2\pi ft)(x_0 - L_1 + L_2 - h)\end{aligned} \tag{43}$$

which describes the displacement dynamics of the downstream meniscus subject to seismic stimulation. A dimensionless form of governing equation (43) is given in Appendix A.

2.4. Numerical Solution Procedure for the Theoretical Model

[42] The momentum balance equation (43) describing the dynamics of the downstream meniscus of a trapped droplet is a second-order nonlinear ordinary differential equation. A fourth-order Runge-Kutta method is used to numerically solve the initial value problem. The initial condition is such that the nonwetting droplet of certain mass is initially trapped in a stable configuration. Its downstream meniscus is, therefore, slightly upstream of the throat of the constriction and is stationary. The initial conditions are given by

$$h = \varepsilon \text{ at } t = 0 \tag{44}$$

$$x_0 = \delta \text{ at } t = 0 \tag{45}$$

$$\frac{\mathrm{d}h}{\mathrm{d}t} = 0 \text{ at } t = 0 \tag{46}$$

where ε and δ are the initial position of the downstream and upstream menisci, respectively.

[43] Since the nonwetting droplet is incompressible, there is also an implicit constraint of volume conservation. To apply it, we need to maintain the volume of the droplet constant. The calculation of the total volume of the droplet is given by

$$V = \frac{\pi(2R_u + d_u)(R_u - d_u)^2}{3} + \frac{\pi(2R_d + d_d)(R_d - d_d)^2}{3} + \pi\int_{x_0}^{h}\big(\lambda(x) - t_f\big)^2\mathrm{d}x \tag{47}$$

$$d_u = c_u - x_0 = \lambda(x_0)\tan\left(\arctan\left(\lambda'(x_0)\right) + \theta_u\right) \tag{48}$$

$$d_d = c_d - h = \lambda(h)\tan\left(\arctan\left(\lambda'(h)\right) + \theta_d\right) \tag{49}$$

which can be obtained by adding the volumes formed by both upstream and downstream menisci and performing volume integration from x_0 to h. In equations (48) and (49), the c_u and c_d are the centers of the upstream and downstream spherical menisci (Figure 1).

[44] At each numerical time step, we solve equation (43) to calculate h first, and then use the bisection method to determine x_0 by numerical iterations of the volume conservation equation (47). Then, we substitute x_0 into equation (43) for the succeeding calculation.

2.5. Computational Fluid Dynamics Simulations

[45] The finite-volume method is used to directly solve the Navier-Stokes equations for two fluids by using the CFD software FLUENT for a comparison with our theoretical model. The two-phase flow in our CFD simulations is described by the incompressible Navier-Stokes equations

$$\begin{cases} \rho\dfrac{\partial}{\partial t}\vec{v} + \rho\nabla\cdot(\vec{v}\vec{v}) = -\nabla P + \mu\nabla\cdot\left(\nabla\vec{v} + \nabla\vec{v}^T\right) + \vec{F} \\ \nabla\cdot\vec{v} = 0 \end{cases} \tag{50}$$

where $\vec{v}$ is the velocity vector; ρ is the density of fluid; μ is the viscosity of fluid; P is the static pressure; $\vec{F}$ is the general body force that includes the volume surface tension $\vec{F}_{\text{vol}}$, and oscillatory fictitious force $-\rho a(t)$ in our simulations.

[46] The volume of fluid (VOF) method [*Hirt and Nichols*, 1981] is used to describe two-phase flow. When solving the flow within each phase, there is no difference between two-phase and single-phase modeling. However, when tracking the interface between multiple phases, the volume fraction equation is used in the VOF model. The volume fraction equation reads as [*Fluent*, 2009]

$$\frac{1}{\rho_q}\left[\frac{\partial}{\partial t}\left(\alpha_q\rho_q\right) + \nabla\cdot\left(\alpha_q\rho_q\vec{v}_q\right) = S_{\alpha_q} + \sum_{p=1}^{n}\left(\dot{m}_{pq} - \dot{m}_{qp}\right)\right] \tag{51}$$

where α_q is the volume fraction of qth fluid; $\dot{m}_{qp}$ is the mass transfer from phase q to phase p; and $\dot{m}_{pq}$ is the mass transfer from phase p to phase q. Both $\dot{m}_{qp}$ and $\dot{m}_{pq}$ are zero in our simulations; there is no mass transfer between nonwetting and wetting fluids and they are immiscible. S_{α_q} is the source term of qth fluid, ρ_q is the density of qth fluid, and $\vec{v}_q$ is the velocity of qth fluid. The volume fraction α_q is defined as follows:

[47] $\alpha_q = 0$: The mesh cell is empty (of the qth fluid).

[48] $\alpha_q = 1$: The mesh cell is full (of the qth fluid).

[49] $0 < \alpha_q < 1$: The mesh cell contains the interface between the qth fluid and one or more other fluids.

[50] $\sum_{q=1}^{n}\alpha_q = 1$: The mesh cell must be filled with either a single fluid phase or a combination of phases.

[51] The fluid properties at the interface are given by

$$\begin{cases} \rho = \sum \alpha_q\rho_q \\ \mu = \sum \alpha_q\mu_q \end{cases} \tag{52}$$

which are volume-fraction-averaged for an n-phase system.

[52] The continuum surface force (CSF) model proposed by *Brackbill et al*. [1992] is used to calculate the curvature of the interface and volume surface tension. In the CSF model, the volume surface force has the following form

$$\vec{F}_{\text{vol}} = \sigma k\nabla\alpha_q \tag{53}$$

where the curvature κ is defined as

$$k = \nabla\cdot\vec{n} \tag{54}$$

where $\vec{n}$ is the unit normal vector of the interface

$$\vec{n} = \frac{\nabla\alpha_q}{|\nabla\alpha_q|} \tag{55}$$

[53] The numerical solution used the following approaches and settings available in FLUENT: The pressure based solver, pressure-implicit with splitting of operators (PISO) for pressure-velocity coupling, least squares cell based for gradient spatial discretization, PRESTO! for pressure spatial discretization, second-order upwind for momentum spatial discretization, Geo-Reconstruct for volume fraction spatial discretization, and first-order explicit scheme for temporal discretization.

[54] The pore geometry and the initially trapped droplet shape are as in Figure 1. The $r_{\max}$ and $r_{\min}$ of the profile equation (1) are 2 and 0.5 mm, respectively. The semiwavelength L is 10 mm for the divergent and convergent part, which is connected to straight tubes upstream and downstream (Figure 1). The total length of the pore is $L_p = 40$ mm. The ε is -0.5 mm and δ is -15 mm. Therefore, the initial length of the droplet is $l_n = 14.5$ mm. The fluid properties are: $\sigma = 0.05$ N/m, $\mu_w = 0.001$ Pa·s, $\mu_n = 0.01$ Pa·s, $\rho_n = 1000$ kg/m^3, and $\rho_w = 1000$ kg/m^3.

[55] We incorporate two different wettability cases: (1) 0° contact angle and (2) 10° contact angle. We assume the nonwetting droplet has been entrapped for a considerably long time and the stable film adsorbed on the mineral wall is nanometers thin [*Gaebel et al*., 2009]. To resolve this, the thin film in the CFD simulations requires an extremely fine numerical mesh and a very long computational time that would render a systematic comparison unfeasible. The film is, therefore, neglected in our comparison of the theoretical model with CFD simulations. Very high-frequency seismic waves in rocks attenuate fast, and only low frequencies are of practical interest for most reservoir and aquifer scenarios. Therefore, we pick relatively low seismic frequencies of 10, 20, 50, and 100 Hz.

3. Results and Discussions

3.1. Comparison With CFD Simulations

[56] The solution of equation (43) is the displacement history of the front meniscus. In order to further analyze the mobilization of trapped droplets, we also present the results for the critical mobilization amplitude A_c at different seismic frequencies and compare it to the results of CFD simulations. To do this, we solve equation (43) for various A and then define A_c as the amplitude of particular acceleration by a seismic wave at which the trapped droplet

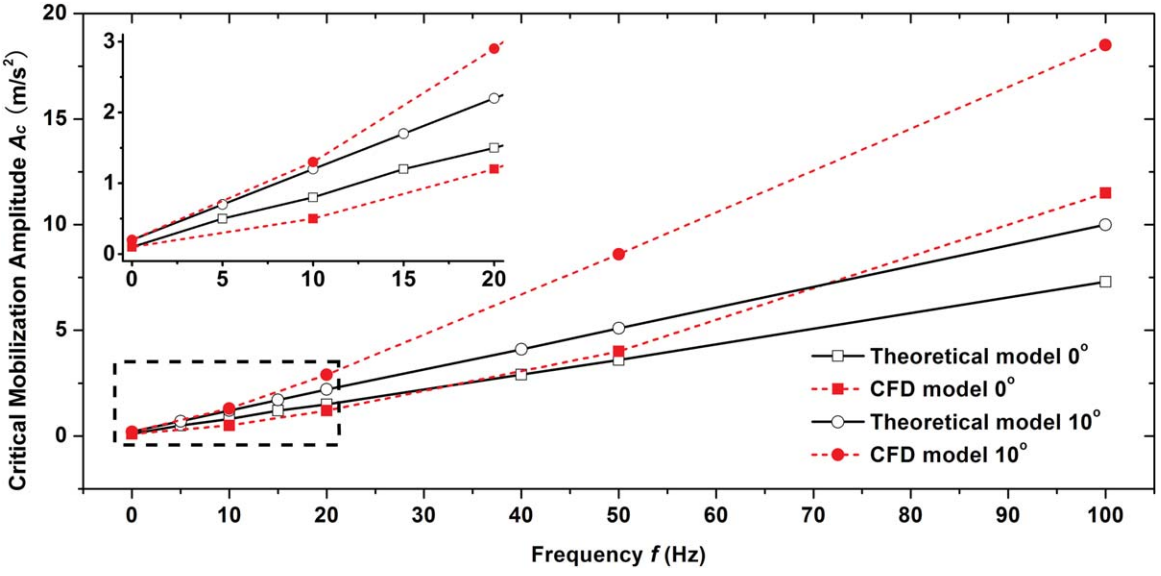

Figure 2. Comparison of the theoretical model to CFD simulations in the prediction of critical mobilization amplitude with contact angles 0° and 10°. The fluid properties are $\sigma = 0.05$ N/m, $\mu_w = 0.001$ Pa·s, $\mu_n = 0.01$ Pa·s, $\rho_n = 1000$ kg/m^3, and $\rho_w = 1000$ kg/m^3.

becomes freed. In addition to frequencies of 10, 20, 50, and 100 Hz for CFD simulations, we also calculated A_c at frequencies of 5, 15, and 40 Hz by using the theoretical model to make the plot of A_c abundant for the theoretical model.

[57] The A_c values we calculated expectedly increased with increasing frequency. Both the theoretical and CFD models show this behavior. When vibration is applied, the general rule is that A_c also increases with the frequency in the absence of resonance [*Beresnev*, 2006; *Beresnev and Deng*, 2010]. When the direction of the oscillatory fictitious force is the same as the flow direction (positive direction), the vibration facilitates the flow; when the oscillatory force reverses direction (negative direction), it resists the flow. It is, therefore, necessary that the vibration stimulates the flow sufficiently within the limited time when flow is in the positive direction in order to free the trapped droplet. This time is controlled by the vibration frequency, thus explaining the larger A_c required at the higher frequency. This dependence on frequency for the seismic mobilization is also consistent with what have been observed in the study of mud volcano dynamics by *Rudolph and Manga* [2012]. In their study, they found that short seismic waves were less effective at influencing mud volcano eruptions than long seismic waves.

[58] We additionally analyze the case of "zero frequency" as the lower limit. In reality, there is no "zero-frequency" seismic wave, so the "zero frequency" case simply represents no vibration. In this case, only a static acceleration is applied to the fluids, like the gravitational acceleration. The A_c value for the "zero frequency" case can be calculated from the Young-Laplace equation based on the mobilization concept [*Beresnev et al.*, 2005]. Any seismic stimulation with its acceleration amplitude less than this value should cause no mobilization of the droplet, no matter what the frequency is [*Beresnev*, 2006]. For this reason, the acceleration amplitude calculated from the static criterion can be called the "threshold" mobilization acceleration A_t. For example, for the droplet trapped by the capillary resistance $\Delta P_c = 2\sigma\ (1/R_d(\varepsilon,\ 0) - 1/R_u(\delta, 0)) = 146$ Pa for the perfect wetting case (0° contact angle), the threshold capillary resistance for the pore is $P_t = 2\sigma\ (1/r_{\min} - 1/r_{\max}) = 150$ Pa when the front meniscus hits the narrowest position at the throat. The threshold acceleration amplitude turns out to be $A_t = (\Delta P_t - \Delta P_e)/\rho L_p = 0.1$ m/s^2 (ΔP_e is the entrapment pressure) (Figure 2).

[59] The A_c calculated with our theoretical model agrees well with the CFD simulations within the frequency range 0–50 Hz for the 0° contact angle case and the frequency range 0–20 Hz for the 10° contact angle case (Figure 2). However, they gradually deviate from the CFD-simulated values as the frequency increases for both cases. One factor leading to this behavior is the assumption of fully developed Hagen-Poiseuille flow profile in the theoretical model. The time scale for the transient Hagen-Poiseuille flow to fully develop in a straight tube is [*Pozrikidis*, 2009]

$$\tau = \frac{\rho r^2}{\mu} \tag{56}$$

where r is the radius of the tube and μ is the viscosity of the fluid. In our case, taking the fluid properties $\rho = 1000$ kg/m^3, $\mu = 0.01$ Pa·s, and $r = 0.5$ mm (when the front is in the pore throat), the time scale τ is 0.025 s (or $1/\tau$ is 40 Hz). Therefore, flow at the frequency higher than approximately 40 Hz does not have a chance to fully develop. The theoretical flow rate calculation which assumes fully developed flow leads to overestimation when the frequency is higher than $1/\tau$ which can be taken as a characteristic frequency, and the corresponding acceleration amplitude of vibration to facilitate the flow is less than it has to be. Hence, the model underestimates A_c at the frequencies higher than roughly 40 Hz. We can clearly observe this trend in Figure 2. However, higher-frequency seismic waves attenuate much faster through reservoirs and are less likely to have any effect on the trapped nonwetting fluids.

If only the lower-frequency waves (e.g., below 40 Hz) are considered, the theoretical model results agree very well with the CFD simulations.

[60] The nonzero contact angle results show larger error in comparison with CFD results than the zero-angle case (Figure 2). This is likely because of our assumption of a spherical shape for the meniscus. We assumed that both front and tail menisci retain their spherical shapes when the droplet is moving. However, in the CFD simulations, we observed changes in the shape of the menisci and apparent contact angles (see supporting information): The front meniscus was more convex than spherical and the tail meniscus was flatter. These shape changes result in an underestimation of the capillary resistance by assuming spherical front and tail menisci in the theoretical model. This shape change effect is similar to the dynamic contact angle effect that the advancing contact angle is less than the static contact angle and the receding contact angle is greater than the static contact angle. Ideally, this shape change effect can be minimized by adding an artificial contact angle correction as an apparent contact angle. Unfortunately, there is no well-vetted model for this apparent contact angle. The nonzero angle case may have a larger error when a constant value of contact angle is assumed instead of adding an apparent contact angle.

[61] It should be noted that the theoretical model, albeit solved numerically, is much more computationally efficient than the direct CFD approach in the prediction of the mobilization amplitudes. The A_c at each frequency is typically obtained after trying less than ten different amplitude values in order to bracket (and eventually converge to) A_c. For the CFD simulations, it takes days to weeks of computing time on a workstation to obtain a single value for A_c. On the other hand, the theoretical model only takes minutes of computing time to obtain the A_c at each frequency. Moreover, for the CFD simulations, the lower the vibration frequency is, the longer is the computational time needed to follow the mobilization because of the longer vibrational period and because the droplet is usually mobilized only after several periods.

[62] Figure 3 presents the history of the response of the trapped droplet (see supporting information for the animations) to seismic stimulation calculated from the theoretical model and the CFD simulation at the frequency 0–50 Hz for 0° contact angle. The droplet oscillates at the same frequency as the seismic frequency. The displacement of the droplet gradually accumulates, usually for several periods of vibration, before the droplet is finally freed. At this stage, the theoretical calculations agree very well with the CFD simulation results at the frequency 0, 10, and 20 Hz (Figures 3a–3c and supporting information). The front slowly passes through the pore throat (0 at the vertical axis where the radius of tube reaches its minimum). Once the front has progressed a certain distance beyond the throat, there is a jump in the displacement, that is, a Haines jump [*Gauglitz and Radke*, 1989], as the droplet is mobilized (see supporting information). After the tail meniscus has passed through the throat, there is a second jump. The theoretical model is identical to the CFD simulation in these details but with minor differences in the exact times of droplet movement. The differences are mainly due to the Haines jump. The velocity predicted by the theoretical model during the Haines jump is greater than the CFD simulation (see the slope 1 of two curves drawn in Figure 3b). After the Haines jump, the velocity of the front meniscus recovers to a quasi steady state. At this stage, the velocity predicted by the theoretical model is close to the CFD simulation (see the slope 2 in Figure 3b). When the second jump occurs, it again leads to a difference in the velocity prediction between the theoretical model and the CFD simulation (see the slope 3 in Figure 3b). A potential explanation can be the effect of the nonspherical shape of droplet menisci as we discussed above. During a Haines jump, the meniscus shape effect has to be more pronounced in order to resist the dramatic velocity change. Since the meniscus shape effect results in an underestimation of capillary resistance, the velocity predicted by the theoretical model during the Haines jump and the second jump is greater than the CFD simulations. Therefore, minor differences in exact times of droplet movement exist in Figures 3a–3c but the periods of vibration before the Haines jumps are the same between the theoretical model and the CFD simulation in Figures 3b and 3c. However, as expected, the theoretical model deviates from the CFD simulation when the frequency (50 Hz) is higher than the characteristic frequency (40 Hz). While it takes ~60 vibration periods to mobilize the droplet in CFD simulation (see supporting information), the mobilization occurs after ~10 vibration periods of stimulation according to the theoretical model (Figure 3d).

[63] The vibration of the droplet before it passes through the pore actually has a phase lag compared to the oscillatory fictitious force. The phase lags are 0.60π, 0.65π, and 0.75π for the 10, 20, and 50 Hz cases, respectively. The theoretical model can capture these phase lags exactly the same as CFD simulations.

[64] The Reynolds numbers in our simulations vary from 1 to 80 during the mobilization process. The higher Reynolds numbers are attributed to the second jump after the tail meniscus passes through the pore throat. Most of the time during the mobilization process, the Reynolds numbers are less than ~10. In this study, the Reynolds number is calculated with the mean velocity and the radius at the pore throat as characteristic velocity and length, respectively. The viscosity and density of the nonwetting fluid are used.

3.2. Comparison With Experiments

[65] We also compare theoretical model calculations to the experimental results reported by *Beresnev et al*. [2011] as well as the previous "viscous seismic model" of *Beresnev and Deng* [2010]. The experiments of *Beresnev et al*. [2011] are the only available laboratory examples directly showing the mobilization of trapped droplets in constricted capillary tubes. In the experiments, a sinusoidally shaped glass tube was manufactured, and one wavelength of this tube was connected to straight sections on both ends (Figure 1). The $r_{\min}$ and $r_{\max}$ of the sinusoidal part were 0.12 and 4.23 mm, and the wavelength was 24.2 mm (the corresponding L in our model is 12.1 mm). The total length of the tube was 114.2 mm with 45 mm straight tubes extending upstream and downstream. The suspended nonwetting fluid had a viscosity μ_n of 0.44×10^{-3} Pa·s, and the viscosity μ_w of the wetting fluid was 0.001 Pa·s. Both fluids had the same density of 998 kg/m^3 which

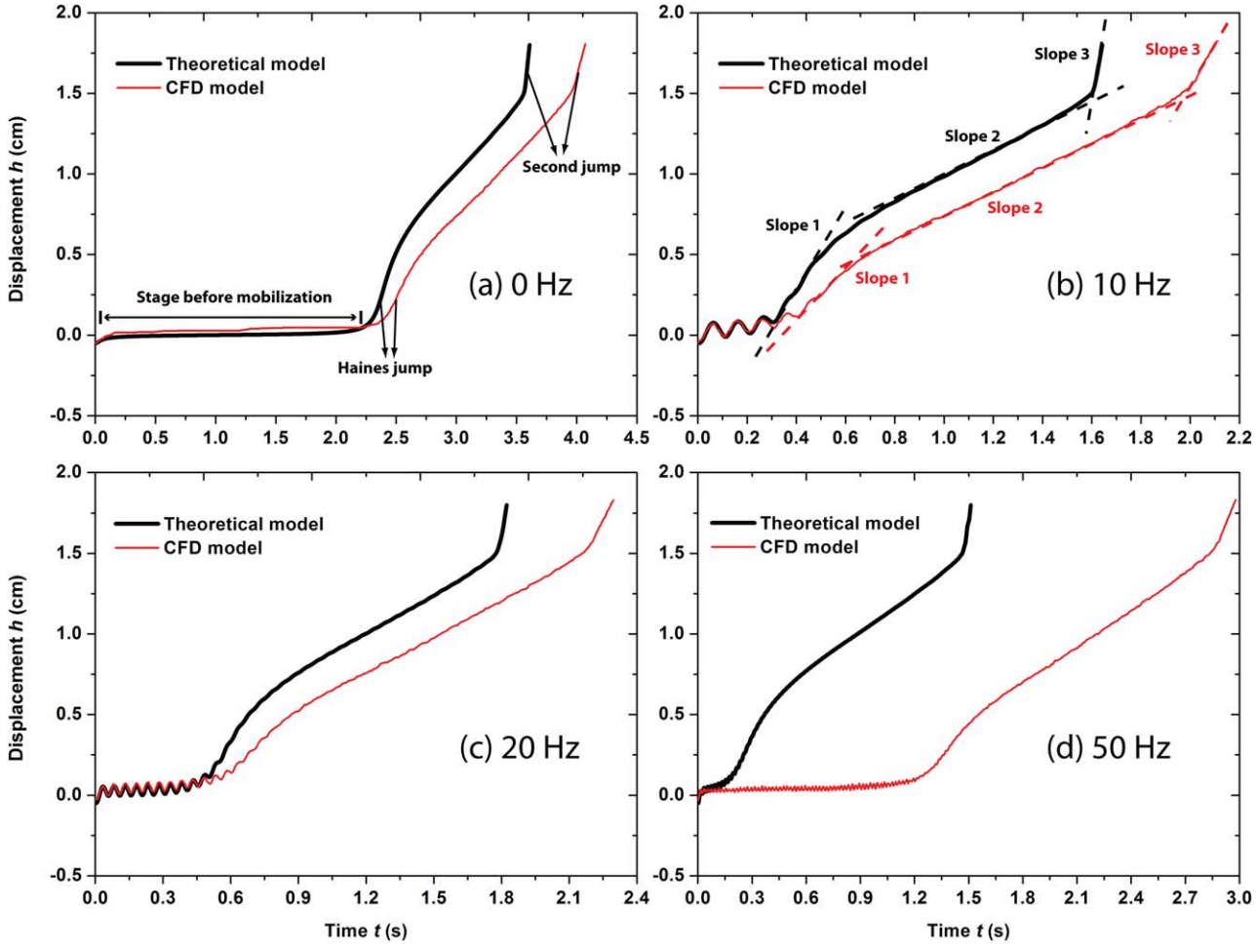

Figure 3. Comparison of theoretical model and CFD simulation calculated transient displacement h of the downstream meniscus with 0° contact angle and different seismic frequency: (a) 0 Hz with acceleration amplitude 0.1 m/s^2; (b) 10 Hz with acceleration amplitude 0.8 m/s^2; (c) 20 Hz with acceleration amplitude 1.5 m/s^2; and (d) 50 Hz with acceleration amplitude 4.0 m/s^2. The acceleration amplitudes in this comparison are from Figure 2. The fluid properties are: $\sigma = 0.05$ N/m, $\mu_w = 0.001$ Pa·s, $\mu_n = 0.01$ Pa·s, $\rho_n = 1000$ kg/m^3, and $\rho_w = 1000$ kg/m^3.

eliminated buoyancy effects. The interfacial tension was 0.016 N/m. The nonwetting ganglion was initially subjected to the entrapment pressure drop ΔP_e along the tube, which was smaller than the threshold ΔP_t required for the mobilization, and the flow, therefore, was initially "plugged." The trapped ganglia were mobilized by the application of vibrations at four different frequencies. The A_c for various cases were recorded. The experimental entrapment and threshold pressure drops, ganglion lengths l_n, critical mobilization amplitude A_c, and the frequencies can be found in *Beresnev et al*. [2011, Table 1]. Noting the l and A_{th} in *Beresnev et al*. [2011, Table 1] are l_n and A_c, respectively, in our study.

Table 1. Comparison Between Experimental Work and Theoretical Solutions in Method (1)[a]

	5 Hz	5 Hz	7.4 Hz	7.4 Hz	10 Hz	14.2 Hz
ΔP_e (Pa)	171	227	206	237	203	183
ΔP_{th} (Pa)	246	246	257	248	248	257
l_n^{lab} (mm)	11.8	11.8	6.4	8.9	8.5	7.9
l_n^{model} (mm)	3.7	4.2	6.9	4.5	4.2	6.8
A_c^{lab} (m/s^2)	0.9	0.7	1.6	0.6	1.3	3.2
A_c^{model} (m/s^2)	0.8	0.3	0.6	0.2	0.6	1

[a]The superscripts "lab" and "model" denote the values measured by laboratory experiments [*Beresnev et al*., 2011] and calculated by our theoretical model, respectively.

[66] The theoretical model cannot simultaneously match the experimentally measured threshold pressure drops and ganglion lengths given in *Beresnev et al*. [2011, Table 1]. According to Young-Laplace equation, the maximum front and tail menisci capillary pressure drop (maximum capillary resistance), which is equal to the threshold pressure drop, is usually reached when the front meniscus resides at the narrowest position of the constriction (pore throat). Therefore, for a given pore geometry and threshold pressure drop, by knowing the radius of the front meniscus at the pore throat, we can calculate the corresponding radius of the tail meniscus by solving the Young-Laplace equation. Subsequently, we can calculate the position of the tail meniscus and the volume of the trapped ganglion. However, given the corresponding entrapment pressure drops,

Table 2. Comparison Between Experimental Work and Theoretical Solutions in Method (2)[a]

	5 Hz	5 Hz	7.4 Hz	7.4 Hz	10 Hz	14.2 Hz
ΔP_e (Pa)	171	227	206	237	203	183
$\Delta P_{th}^{\text{lab}}$ (Pa)	246	246	257	248	248	257
$\Delta P_{th}^{\text{model}}$ (Pa)	259	259	255	258	258	257
l_n (mm)	11.8	11.8	6.4	8.9	8.5	7.9
A_c^{lab} (m/s^2)	0.9	0.7	1.6	0.6	1.3	3.2
A_c^{model} (m/s^2)	0.9	0.4	0.6	0.3	0.7	1

[a]The superscripts "lab" and "model" denote the values measured by laboratory experiments [*Beresnev et al*., 2011] and calculated by our theoretical model, respectively.

we cannot theoretically get the same lengths of trapped ganglion as reported in *Beresnev et al*. [2011, Table 1] by calculating the volume of the trapped ganglia. Therefore, the documented threshold pressure drops and ganglion lengths from the experiments, as reported, appear to be not internally consistent and suggest some level of error in the measurements. In light of this, we use two methods to accomplish our comparison: (1) we assume that the entrapment and threshold pressure drops are correct in the experiment, but allow deviation in the exact length of the trapped ganglion; (2) we assume that the entrapment pressure drop and the length are correct in the experiment, but allow deviation in the threshold pressure drop. In method (1), therefore, we first put the front meniscus at the throat of the pore, and then calculate the radius of the tail meniscus and its position to match the experimentally measured threshold pressure drop from *Beresnev et al*. [2011, Table 1] by solving equation (3). Then, in the theoretical model, we set the experimentally measured entrapment pressure drop from *Beresnev et al*. [2011, Table 1] and calculate the equilibrium position and length of the ganglion as summarized in Table 1. The lengths of the trapped ganglia are within a factor of 1–3 of the experimental measurements. In method (2), we take the experimental length of the ganglion from *Beresnev et al*. [2011, Table 1] and entrap the ganglion at the experimental entrapment pressure drop from *Beresnev et al*. [2011, Table 1]. Then, we gradually increase the external pressure drop until the ganglion is mobilized and thus obtain the threshold pressure drop as summarized in Table 2. Our comparisons showed a maximum 5% difference with the experimental measurements. The comparison of l_n^{lab} and l_n^{model} in Table 1 and $\Delta P_{th}^{\text{lab}}$ and $\Delta P_{th}^{\text{model}}$ in Table 2 indicates some internal inconsistencies in the experimental results.

[67] Using CFD simulations following method (2), we also modeled two cases for further comparison with the theoretical model; the cases considered are the lowest frequency case "5 Hz, 171 Pa" and the highest frequency case "14.2 Hz, 183 Pa." Figure 4 shows the comparison of the mobilization accelerations predicted by experiments of *Beresnev et al*. [2011], our theoretical model following methods (1) and (2), CFD simulations following method (2), and the viscous seismic model. In the case "5 Hz, 171 Pa," the A_c calculated by CFD simulation and theoretical model following method (2) are exactly the same, while the A_c calculated by CFD simulation slightly deviates from theoretical model for the high-frequency case "14.2 Hz, 183 Pa." The theoretical model, especially when applied with method (2), agrees better with the experiment (Figure 4) than the viscous model in five out of six cases. The errors are from 0% to 70%. Moreover, in relation to the viscous seismic model, the new theory has the additional advantage of satisfying volume conservation instead of assuming a constant length for the moving ganglion. The latter assumption is only strictly valid when the slope of the tube profile is very gentle such that the displacement of the ganglion will not result in a significant change in its length. Furthermore, the new model comprehensively represents the momentum balance for the nonwetting phase. Thus, the new model expectedly performs much better than the viscous seismic model in most cases, although the governing equation (43) that needs to be solved is more complex than the corresponding equation of the viscous seismic model. However, as the comparison with the CFD simulation shows, the new theory still systematically underestimates A_c as the vibration frequency increases.

4. Summary and Conclusions

[68] We developed a new theoretical model that describes the response of two-phase flow to oscillatory forcing created by a seismic wave passing a porous medium. The development follows a comprehensive analysis of momentum balance and volume conservation in a moving-boundary control volume representing a droplet trapped behind a pore constriction. The final result is a comprehensive force balance equation whose solution gives the displacement of the front meniscus of the trapped droplet; the equation is a second-order nonlinear ordinary differential equation which needs to be numerically solved. The model can, therefore, be used not only to predict the location of the front but also to investigate whether the droplet completely passes through the trapping pore constriction and becomes dislodged. The droplet mobilization predicted by the model was validated by favorable

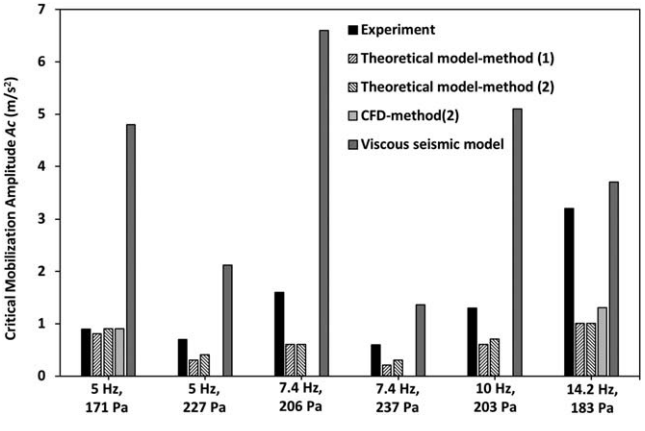

Figure 4. Comparison of the critical mobilization amplitudes calculated by: experiments of *Beresnev et al*. [2011], the theoretical model with methods (1) and (2), the CFD calculation with method (2) and viscous seismic model of *Beresnev and Deng* [2010]. The comparison is made for different frequency and pressure.

comparison against complete CFD simulations and previously available experimental data.

[69] The model was also used to determine at which seismic wave amplitude, for a given frequency, the droplet becomes dislodged. Comparison of the critical mobilization amplitudes calculated by the theoretical model with results of two-phase CFD simulations demonstrates accurate performance of our theoretical model in the low-frequency range below a characteristic frequency. This characteristic frequency can be approximated by the time it takes for Hagen-Poiseuille flow to fully develop. The theoretical model agrees better with the CFD simulations for the case of 0° contact angle than for a nonzero one, possibly due to the apparent contact angle effect. Good agreement of the droplet displacement history between the model and the CFD simulation (for droplets exposed to lower stimulation frequencies) highlights the accuracy of the theory in terms of describing the complex seismically induced two-phase flow. By comparing to experimental data, our new theory shows better prediction of the critical mobilization amplitude than a previous "viscous seismic model."

[70] Our model simplifying the two-phase flow problem is computationally much more efficient than a complete solution of the Navier-Stokes equations done through a CFD simulation. For example, it takes days to weeks to find a single mobilization amplitude for a droplet by trial and error, especially at low frequencies, in CFD simulations. On the other hand, this only takes minutes with the theoretical model which is also solved numerically.

[71] To conclude, we developed a new comprehensive theoretical model that is effective and robust in describing the dynamics of droplets subject to the passage of seismic waves in constricted tubes. This model can be effectively used to predict the dislodgement of trapped droplets and can potentially be used to explain seismically induced permeability change in reservoirs and aquifers.

Appendix A

[72] The dimensionless form of the governing equation (43) is

$$
\begin{aligned}
&a_p\left[h^* - x_0^* + \frac{2}{3}\left(\lambda^*\left(x_0^*\right) + \lambda^*(h^*) - 2t_f^*\right)\right]\frac{\mathrm{d}^2h^*}{\mathrm{d}t^{*2}} \\
&+a_\rho\left(1 - \frac{\left(\lambda^*(h^*) - t_f^*\right)^2}{\left(\lambda^*(x_0) - t_f^*\right)^2}\right)\left(\frac{\mathrm{d}h^*}{\mathrm{d}t^*}\right)^2 + 8a_\mu\cdot\mathrm{Oh}\cdot \\
&\mathrm{int}1^*(h^*)\frac{\mathrm{d}h^*}{\mathrm{d}t^*} = \Delta P_e^* - 2\left(\frac{1}{R_d^*(h^*,\theta_d)} - \frac{1}{R_u^*\left(x_0^*,\theta_u\right)}\right) \qquad \text{(A1)} \\
&-\frac{8\cdot\mathrm{Oh}}{\pi}S^*(h^*)\frac{\mathrm{d}h^*}{\mathrm{d}t^*} \\
&\left(\int_{L_1^*}^{x_0^*}\frac{1}{\lambda^{*4}(x^*)}\mathrm{d}x^* + \int_{h^*}^{L_2^*}\frac{1}{\lambda^{*4}(x^*)}\mathrm{d}x^*\right) - 2c^*\cdot\mathrm{int}\,3^*(h^*) \\
&+a_\rho A^*\cdot\sin\left(2\pi f^*t^*\right)\left(h^* - x_0^*\right)+ \\
&A^*\cdot\sin\left(2\pi f^*t^*\right)\left(x_0^* - L_1^* - L_2^* - h^*\right)
\end{aligned}
$$

where the dimensionless variables and parameters are

$$
\begin{aligned}
&x^* = \frac{x}{r_{\min}}, h^* = \frac{h}{r_{\min}}, x_0^* = \frac{x_o}{r_{\min}}, t_f^* = \frac{t_f}{r_{\min}}, L_1^* = \frac{L_1}{r_{\min}}, \\
&L_2^* = \frac{L_2}{r_{\min}}, \lambda^*(x^*) = \frac{\lambda(x)}{r_{\min}}, R_d^*(h^*,\theta_d) = \frac{R_d(h,\theta_d)}{r_{\min}}, \\
&R_u^*\left(x_0^*\right) = \frac{R_{u\left(x_0,\theta_d\right)}}{r_{\min}}, \mathrm{int}\,1^*(h^*) = \frac{\mathrm{int}\,1(h)}{\frac{1}{r_{\min}}}, \\
&\mathrm{int}\,3^*(h^*) = \frac{\mathrm{int}\,3(h)}{\frac{1}{r_{\min}}}, S^*(h^*) = \frac{s(h)}{r_{\min}^2}, c^* = \frac{c}{\sigma}, t^* = \frac{t}{\left(\rho_w r_{\min}^3/\sigma\right)^{1/2}}, \\
&\Delta P_e^* = \frac{\Delta P_e}{\frac{\sigma}{r_{\min}}}, A* = \frac{A}{\frac{\sigma}{\rho_w r_{\min}^2}}, f^* = \frac{f}{\left(\frac{\sigma}{\rho_w r_{\min}^3}\right)^{1/2}}, \\
&\mathrm{Oh} = \frac{\mu_w}{\left(\rho_w\sigma r_{\min}\right)^{1/2}}, a_\rho = \frac{\rho_n}{\rho_w}, a_\mu = \frac{\mu_n}{\mu_w}
\end{aligned}
$$

[73] The important dimensionless parameters in equation (A1) are: the Ohnesorge number Oh which relates the viscous forces to inertial and surface tension forces, the density ratio a_ρ, the viscosity ratio a_μ, the entrapment pressure drop ΔP_e^*, the acceleration amplitude A^*, the seismic frequency f^*, and the tube geometry $\lambda^*(x^*)$. In our theoretical model and CFD simulation comparison, the Oh is 0.0063, the a_ρ is 1, and the a_μ is 10. In the experimental work of *Beresnev et al*. [2011] and our comparison, the Oh is 0.023, the a_ρ is 1, and the a_μ is 0.44.

[74] **Acknowledgments.** This material is based upon work supported as part of the Center for Frontiers of Subsurface Energy Security (CFSES) at the University of Texas at Austin, an Energy Frontier Research Center funded by the U.S. Department of Energy, Office of Science, Office of Basic Energy Sciences under award DE-SC0001114. Additional support was provided by the Geology Foundation of the University of Texas. The data and information of laboratory experiments in this study were provided by Igor Beresnev and Dennis Vigil. The authors are grateful to Igor Beresnev for fruitful discussions and for reviewing an earlier version of this paper. We thank Michael Manga and an anonymous reviewer for their help in improving our manuscript.

References

Beckham, R. E., A. I. Abdel-Fattah, P. M. Roberts, R. Ibrahim, and S. Tarimala (2010), Mobilization of colloidal particles by low-frequency dynamic stress stimulation, *Langmuir*, *26*(1), 19–27.

Beresnev, I. A. (2006), Theory of vibratory mobilization on nonwetting fluids entrapped in pore constrictions, *Geophysics*, *71*(6), N47–N56.

Beresnev, I. A., and W. Deng (2010), Viscosity effects in vibratory mobilization of residual oil, *Geophysics*, *75*(4), N79–N85.

Beresnev, I. A., and P. A. Johnson (1994), Elastic-wave stimulation of oil production: A review of methods and results, *Geophysics*, *59*(6), 1000–1017.

Beresnev, I. A., R. D. Vigil, W. Q. Li, W. D. Pennington, R. M. Turpening, P. P. Iassonov, and R. P. Ewing (2005), Elastic waves push organic fluids from reservoir rock, *Geophys. Res. Lett.*, *32*, L13303, doi:10.1029/2005GL023123.

Beresnev, I., W. Gaul, and R. D. Vigil (2011), Direct pore-level observation of permeability increase in two-phase flow by shaking, *Geophys. Res. Lett.*, *38*, L20302, doi:10.1029/2011GL048840.

Brackbill, J. U., D. B. Kothe, and C. Zemach (1992), A continuum method for modeling surface tension, *J. Comput. Phys.*, *100*(2), 335–354.

Dobronravov, O. V. (2002), Industry feature: A new technology of reservoir stimulation through exposure to weak seismic waves, *First Break*, *20*(6), 376–382.

Elkhoury, J. E., E. E. Brodsky, and D. C. Agnew (2006), Seismic waves increase permeability, *Nature*, *441*(7097), 1135–1138.

Elkhoury, J. E., A. Niemeijer, E. E. Brodsky, and C. Marone (2011), Laboratory observations of permeability enhancement by fluid pressure

oscillation of in situ fractured rock, *J. Geophys. Res.*, *116*, B02311, doi:10.1029/2010JB007759.

Fluent (2009), User's guide, ANSYS Fluent 12.0.

Gaebel, C., J. R. Lead, J. C. Renshaw, and J. H. Tellam (2009), Preliminary indications from atomic force microscopy of the presence of rapidly-formed nanoscale films on aquifer material surfaces, *J Contam. Hydrol.*, *108*(1–2), 46–53.

Gauglitz, P. A., and C. J. Radke (1988), An extended evolution equation for liquid film breakup in cylindrical capillaries, *Chem. Eng. Sci.*, *43*, 1457–1465.

Gauglitz, P. A., and C. J. Radke (1989), Dynamics of Haines jumps for compressible bubbles in constricted capillaries, *AIChE J.*, *35*(2), 230–240.

Gauglitz, P. A., and C. J. Radke (1990), The dynamics of liquid-film breakup in constricted cylindrical capillaries, *J. Colloid Interface Sci.*, *134*(1), 14–40.

Geballe, Z. M., C. Y. Wang, and M. Manga (2011), A permeability-change model for water-level changes triggered by teleseismic waves, *Geofluids*, *11*(3), 302–308.

Graham, D. R., and J. J. L. Higdon (2000), Oscillatory flow of droplets in capillary tubes. Part 2. Constricted tubes, *J. Fluid Mech.*, *425*, 55–77.

Hilpert, M. (2007), Capillarity-induced resonance of blobs in porous media: Analytical solutions, Lattice-Boltzmann modeling, and blob mobilization, *J. Colloid Interface Sci.*, *309*(2), 493–504.

Hilpert, M., G. H. Jirka, and E. J. Plate (2000), Capillarity-induced resonance of oil blobs in capillary tubes and porous media, *Geophysics*, *65*(3), 874–883.

Hirt, C. W., and B. D. Nichols (1981), Volume of fluid (VOF) method for the dynamics of free boundaries, *J. Comput. Phys.*, *39*(1), 201–225.

Iassonov, P. P., and I. A. Beresnev (2003), A model for enhanced fluid percolation in porous media by application of low-frequency elastic waves, *J. Geophys. Res.*, *108*(B3), 2138, doi:10.1029/2001JB000683.

Iassonov, P. P., and I. A. Beresnev (2008), Mobilization of entrapped organic fluids by elastic waves and vibrations, *SPE J.*, *13*(4), 465–473.

Kouznetsov, O. L., E. M. Simkin, G. V. Chilingar, and S. A. Katz (1998), Improved oil recovery by application of vibro-energy to waterflooded sandstones, *J. Petrol. Sci. Eng.*, *19*, 191–200.

Li, W. Q., R. D. Vigil, I. A. Beresnev, P. Iassonov, and R. Ewing (2005), Vibration-induced mobilization of trapped oil ganglia in porous media: Experimental validation of a capillary-physics mechanism, *J. Colloid Interface Sci.*, *289*(1), 193–199.

Liu, W. Q., and M. Manga (2009), Changes in permeability caused by dynamic stresses in fractured sandstone, *Geophys. Res. Lett.*, *36*, L20307, doi:10.1029/2009GL039852.

Manga, M., I. Beresnev, E. E. Brodsky, J. E. Elkhoury, D. Elsworth, S. E. Ingebritsen, D. C. Mays, and C.-Y. Wang (2012), Changes in permeability caused by transient stresses: Field observations, experiments, and mechanisms, *Rev. Geophys.*, *50*, RG2004, doi:10.1029/2011RG000382.

Middleman, S. (1995), *Modeling Axisymmetric Flows: Dynamics of Films, Jets, and Drops*, Academic, London, UK.

Nikolaevskiy, V. N., G. P. Lopukhov, Y. Liao, and M. J. Economides (1996), Residual oil reservoir recovery with seismic vibrations, *SPE Prod. Facil.*, *5*, 89–94.

Poesio, P., G. Ooms, S. Barake, and F. van der Bas (2002), An investigation of the influence of acoustic waves on the liquid flow through a porous material, *J. Acoust. Soc. Am.*, *111*, 2019–2025.

Pozrikidis, C. (2009), *Fluid Dynamics: Theory, Computation, and Numerical Simulation*, Springer, New York, USA.

Pride, S. R., E. G. Flekkoy, and O. Aursjo (2008), Seismic stimulation for enhanced oil recovery, *Geophysics*, *73*(5), O23–O35.

Roberts, P. M. (2005), Laboratory observations of altered porous fluid flow behavior in Berea sandstone induced by low-frequency dynamic stress stimulation, *Acoust. Phys.*, *51*, 160–168.

Roberts, P. M., and A. I. Abdel-Fattah (2009), Seismic stress stimulation mobilizes colloids trapped in a porous rock, *Earth Planet. Sci. Lett.*, *284*(3–4), 538–543.

Roberts, P. M., I. B. Esipov, and E. L. Majer (2003), Elastic wave stimulation of oil reservoirs: Promising EOR technology?, *Leading Edge*, *5*, 448–453.

Roberts, P. M., A. Sharma, V. Uddameri, M. Monagle, D. E. Dale, and L. K. Steck (2001), Enhanced DNAPL transport in a sand core during dynamic stress stimulation, *Environ. Eng. Sci.*, *18*(2), 67–79.

Rudolph, M. L., and M. Manga (2012), Frequency dependence of mud volcano response to earthquakes, *Geophys. Res. Lett.*, *39*, L14303, doi:10.1029/2012GL052383.

Thomas, M., and C. V. Chrysikopoulos (2007), Experimental investigation of acoustically enhanced colloid transport in water-saturated packed columns, *J. Colloid Interface Sci.*, *308*(1), 200–207.

Wang, C. Y., and M. Manga (2010), Hydrologic responses to earthquakes and a general metric, *Geofluids*, *10*(1–2), 206–216.

Zoback, M. D., and S. M. Gorelick (2012), Earthquake triggering and large-scale geologic storage of carbon dioxide, *Proc. Natl. Acad. Sci. U. S. A.*, *109*(26), 10164–10168, doi:10.1073/pnas.1202473109.